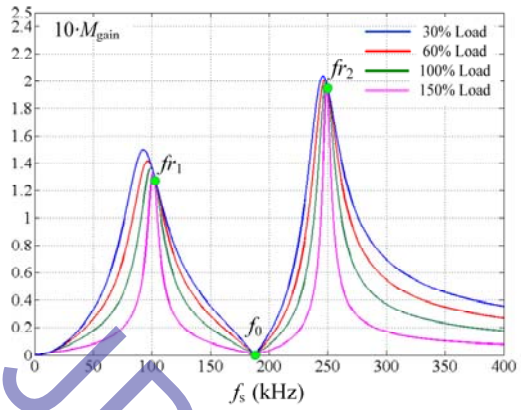

Fig. 6. Voltage gain curves at different loads.

A. Circuit Modelling

A FHA model of the dual-CLT converter is constructed as shown in Fig. 5. E_i and E_o are the fundamental components of the input and output voltages of the resonant tank. I_1, I_2 and I_{C2} are the currents through L_1, L_2 and C_2. In addition, I_{s1} and I_{s2} are the secondary currents of T_1 and T_2. Furthermore, R_{eq} is the equivalent ac load of the resistor R_o. Meanwhile, V_{T1} and V_{T2} are the primary voltages of T_1 and T_2. List the KCL / KVL equations as (5), and the dc voltage gain M_{gain} can be deduced.

$$\begin{cases} E_i = I_1 \cdot (sL_1 + \dfrac{1}{sC_1}) + V_{T1} + I_2 \cdot sL_2 + V_{T2} \\ I_{C2} \cdot \dfrac{1}{sC_2} = I_2 \cdot sL_2 + V_{T2} \\ I_1 = I_2 + I_{C2} \\ V_{T1} = N_1 \cdot E_o \\ V_{T2} = N_2 \cdot E_o \\ I_1 = \dfrac{V_{T1}}{sL_{m1}} + \dfrac{I_{S1}}{N_1} \\ I_2 = \dfrac{V_{T2}}{sL_{m2}} + \dfrac{I_{S2}}{N_2} \\ E_o = R_{eq} \cdot (I_{S1} + I_{S2}) \\ R_{eq} = \dfrac{8}{\pi^2} R_o \end{cases} \tag{5}$$

Then, based on $s = j \cdot \omega_s$, where ω_s is the relevant angular frequency of the operating frequency f_s, it is possible to express M_{gain} as:

$$M_{gain} = \left| \frac{1}{M_{Re} + jM_{Im}} \right| = \left| \frac{1}{(C_\omega + \dfrac{A_\omega B_\omega}{C_\omega}) + j\dfrac{A_\omega R_{eq}}{C_\omega}} \right| \tag{6}$$

$$\begin{cases} A_\omega = \omega_s L_1 - \dfrac{1}{\omega_s C_1} + \dfrac{\omega_s L_2}{1 - \omega_s^2 C_2 L_2} \\ B_\omega = \dfrac{N_1^2}{\omega_s L_{m1}} + \dfrac{N_2^2}{\omega_s L_{m2}} - \dfrac{\omega_s C_2 N_2^2}{1 - \omega_s^2 C_2 L_2} \\ C_\omega = N_1 + \dfrac{N_2}{1 - \omega_s^2 C_2 L_2} \end{cases} \tag{7}$$

From (6)-(7), the M_{gain} curves with different loads are drawn in Fig. 6. This indicates that the dual-CTL converter has two resonant frequency points f_{r1} and f_{r2} as well as a RZP f_0, at which M_{gain} is kept constant. The converter should be operated within the frequency scope from f_{r1} to f_0, where ZVS turning on is guaranteed for the power switches. This narrow range (f_{r1}, f_0) also contributes to a broadened voltage gain range.

In addition, from (6), the expressions of the resonant points are calculated as:

$$f_{r1} = \frac{1}{2\pi} \sqrt{\frac{L_1C_1 + L_2C_2 + L_2C_1 - \sqrt{(L_1C_1 + L_2C_2 + L_2C_1)^2 - 4L_1C_1L_2C_2}}{2L_1C_1L_2C_2}} \tag{8}$$

$$f_{r2} = \frac{1}{2\pi} \sqrt{\frac{L_1C_1 + L_2C_2 + L_2C_1 + \sqrt{(L_1C_1 + L_2C_2 + L_2C_1)^2 - 4L_1C_1L_2C_2}}{2L_1C_1L_2C_2}} \tag{9}$$

$$f_0 = \frac{1}{2\pi} \sqrt{\frac{1}{C_2L_2}} \tag{10}$$

B. MATLAB Program Filtration

Based on a FHA model, MATLAB is employed to filter the resonant parameters for the first step. From (6)-(10), total of six parameters needs to be selected, including C_1, C_2, L_1, L_2 and the turns ratios N_1 and N_2 of T_1 and T_2.

Since the secondary sides of T_1 and T_2 are connected in parallel, as shown in Fig. 1, for most of the time, their voltages V_{T1} and V_{T2} are clamped by the dc output voltage V_{out} and do not participate in the resonance. Thus, in this paper, the magnetizing inductors L_{m1} and L_{m2} of T_1 and T_2 are chosen for a comprehensive consideration of the circulating energy and the core volume. Small values of L_{m1} and L_{m2} increase the transformer losses, while larger values lead to a larger size and a lower power density.

Then, depending on the practical engineering issues, each of these six parameters is given a pre-set wide range. These ranges cover all of the reasonable parameter values. Every variable varies within its given range from the lowest to the highest at a small fixed step. The scopes and steps of these variables are listed in Table I.

Define GRi (i = 1, 2, 3, …) as a parameter group. Every GRi is a combination of the six variables {L1, L2, C1, C2, N1, N2}, and each variable has a certain value. Every GRi is unique and different from the others. Thus, the GRi acts as the fundamental element for the following design procedures.

TABLE I
RANGES AND STEPS FOR THE RESONANT PARAMETERS

Resonant Parameter	Range		Step
Turns Ratios N_1	1	8	0.5
Turns Ratios N_2	1	8	0.5
Inductor L_1	10μH	300μH	10μH
Inductor L_2	10μH	300μH	10μH
Capacitor C_1	3nF	30nF	3nF
Capacitor C_2	3nF	30nF	3nF

MATLAB mainly verifies if a certain GR_i is consistent with the selection constraints. Group GR_{Si} (i = 1, 2, 3, …), which satisfies the constraints, are recorded, while others are automatically abandoned by the program. As a result, all of the satisfactory groups of GR_{Si} are able to ensure acceptable MERC resonant performances.

The selection constraints for the dual-CTL circuit are listed below.

1) $f_{r1} < f_0 < f_{r2}$. Based on (8)-(10), the resonant points should to be arranged properly, so that the M_{gain} curves can match well with Fig. 6. The converter achieves a widely adjustable voltage gain within the narrow frequency range from f_{r1} to f_0.

2) 98kHz < f_{r1} < 102kHz. The rating point f_{sr} is set at 100kHz. Because f_{sr} is supposed to closely approach f_{r1} for loss reduction, f_{r1} should meet this inequation.

3) 150kHz < f_0 < 180kHz. The location of f_0 must be considered carefully, since it is significant for a RZP-MERC. If f_0 is near f_{r1}, M_{gain} can be modulated flexibly with a small frequency scope. In addition, the circulating energy increases as the detrimental outcomes when f_0 is too closed to f_{r1}. Hence, f_0 is set among (150kHz, 180kHz) for a compromise [24].

4) Rating voltage gain requirement. To meet the demands of the rating voltages, $M_{gain}(f_{r1})$ needs to be designed. Here V_{in} = 400V, V_{out} = 52V. Thus, $M_{gain}(f_{r1})$ is located around 0.13.

5) Leakage inductor requirement. For practical engineering considerations, leakage inductors are generally 3% to 5% of their magnetizing inductors [15]. Hence, L_1 and L_2 must be larger than 5% of L_{m1} and L_{m2}, respectively.

A flow chart of MATLAB is shown in Fig. 7. After filtration, the satisfactory groups GR_{Si} are picked out from the large parameter ranges of Table I to the more limited ranges.

C. Conduction Loss and Turn-Off Loss

For every GR_{Si}, the conduction loss and turn-off loss are investigated in this section to determine a trade-off group $GR_{S\text{-}TO}$.

The conduction losses are mainly composed of the primary-side loss and the secondary-side loss. For the latter,

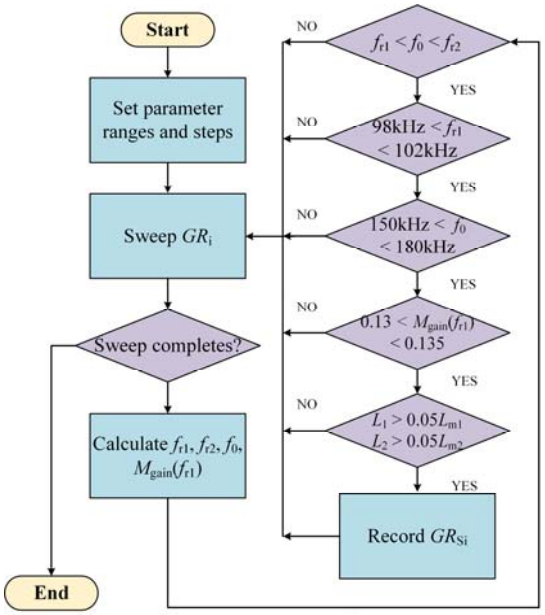

Fig. 7. Flow chart of MATLAB.

the square-shape voltage waveform of the SR is exactly in phase with the SR's sine current waveform. This is because the equivalent topology of the SR is altered when its current is equal to zero and flows to the opposite direction. Therefore, the secondary-side conduction loss is positively proportional to the output current, which is only decided based on the load condition, and has a weak correlation with the resonant parameters. On the other hand, for the primary side, the voltage and current of the resonant tank are not exactly in phase with each other due to the input impedance Z_{in}. Z_{in} is decided by the resonant tank. Therefore, the relation between the primary-side conduction loss P_{conS} and resonant parameters should be analyzed. P_{conS} is expressed as (11), where T_s is the switching period, r_{DS} is the conduction resistance of the MOSFET switch and $i_{S1}(t)$ is the current through S_1.

$$P_{conS} = 2 \cdot \frac{1}{2} \cdot \frac{2}{T_s} \int_0^{\frac{T_s}{2}} r_{DS} i_{S1}^2(t) dt \tag{11}$$

Based on the FHA analysis, when S_1 turns on, a sinusoidal current can be used to substitute $i_{S1}(t)$ for the approximation in [6]. Hence, (11) is converted to:

$$P_{conS} \approx r_{DS} I_{1\text{-rms}}^2 \tag{12}$$

Where $I_{1\text{-rms}}$ represents the RMS current of L_1. From (12), it can be inferred that a smaller $I_{1\text{-rms}}$ is preferred in order to limit P_{conS}. $I_{1\text{-rms}}$ and Z_{in} are deduced as (13)-(15).

$$I_{1\text{-rms}} = \frac{\sqrt{2} V_{in}}{\pi Z_{in}} \tag{13}$$

$$Z_{in} = Z_{Re} + j \cdot Z_{Im} \tag{14}$$

$$\begin{cases} Z_{\mathrm{Re}} = \dfrac{R_{\mathrm{eq}} C_{\omega}^2}{1 + R_{\mathrm{eq}}^2 B_{\omega}^2} \\ Z_{\mathrm{Im}} = A_{\omega} + \dfrac{R_{\mathrm{eq}}^2 C_{\omega}^2 B_{\omega}}{1 + R_{\mathrm{eq}}^2 B_{\omega}^2} \end{cases} \tag{15}$$

The turn-off loss is dominated by the turn-off current I_{turnoff}, which is derived as:

$$I_{\mathrm{turnoff}} = \left| \sqrt{2} I_{\mathrm{1\text{-}rms}} \sin(\pi - \varphi_{\mathrm{in}}) \right| = \left| \sqrt{2} I_{\mathrm{1\text{-}rms}} \sin(\varphi_{\mathrm{in}}) \right| \tag{16}$$

Where φ_{in} is the input impedance angle of the resonant tank. φ_{in} is

$$\varphi_{\mathrm{in}} = \arctan\left(\frac{Z_{\mathrm{Im}}}{Z_{\mathrm{Re}}}\right) \tag{17}$$

Equation (16) demonstrates that the turn-off loss presents a positive correlation with φ_{in}. Thus, to limit the turn-off loss, φ_{in} should be confined. In this case, φ_{in} at $f_s = 1.1 f_{r1}$ is employed to reflect the turn-off loss for the primary-side switches.

Calculate $I_{\mathrm{1\text{-}rms}}$ and φ_{in} for each of the GR_{Si}. Then, rank the groups, from the group $GR_{\mathrm{S\text{-}LCL}}$ with the lowest P_{conS} to the group with the highest P_{conS}. Due to a limited article space, only a part of the results is listed in Table II. From this table, the trade-off group $GR_{\mathrm{S\text{-}TO}}$ can be achieved, and the corresponding parameters are listed as L_1 =200μH, L_2 = 140μH, C_1 = 6nF, C_2 = 6nF, N_1 = 1.5 and N_2 = 1.5. Although $GR_{\mathrm{S\text{-}TO}}$ elevates $I_{\mathrm{1\text{-}rms}}$ slightly resulting in a 1% promotion of P_{conS}, φ_{in} reduces 37% when compared with $GR_{\mathrm{S\text{-}LCL}}$. This contributes to much lower turn-off losses. Therefore, $GR_{\mathrm{S\text{-}TO}}$ is chosen in this step.

Since the $GR_{\mathrm{S\text{-}TO}}$ has already been decided, the reasonable ranges for the resonant parameters are further confined. Centering on the parameter values of the $GR_{\mathrm{S\text{-}TO}}$, each of the six resonant parameters is limited within the range from the upper step to the lower step. Nevertheless, the large number of parameters makes it very difficult to conduct the following optimization. Hence, for simplification, some of the parameters are determined first and the remaining parameters are further fine-tuned through 3D figures. By this means, although deviations are inevitably introduced, they can be slight and negligible due to the very limited parameter scopes. Here, the parameters of the transformers are preset. At the same time, the ranges for the remaining parameters are obtained as: L_1 (200μH ± 10μH), L_2 (140μH ± 10μH), C_1 (6nF± 3nF) and C_2 (6nF± 3nF).

D. 3D Figure Fine-Tuning

The 3D figures are drawn according to the deduced expressions of different RCVs, including φ_{in}, M_{gain} and the ac voltage stresses V_{C1} and V_{C2} of the capacitor C_1 and C_2. These 3D figures reflect the variation trends between the RCVs and the resonant parameters. Since the borders of these figures were determined at the end of *Part C*, the main objective of this step is to fine-tune the parameters.

TABLE II
PARTIAL SELECTION RESULTS OF MATLAB

L_1 (μH)	L_2 (μH)	C_1 (nF)	C_2 (nF)	N_1	N_2	$I_{\mathrm{1\text{-}rms}}$ (A)	φ_{in}
110	70	12nF	12	1.5	1.5	2.8913	0.83
120	90	9nF	12	2	1	2.8916	0.76
250	90	6	9	2	1	2.8921	0.71
50	60	18	15	1.5	1.5	2.8924	0.74
30	90	15	9	1.5	1.5	2.8928	0.78
200	140	6	6	1.5	1.5	2.8930	0.60
210	50	9	18	2	1	2.8933	0.82
20	220	6	3	1.5	1.5	2.8934	0.71
290	90	6	9	1.5	1.5	2.8938	0.69
80	120	9	9	2	1	2.8940	0.75
60	90	12	12	2	1	2.8943	0.70
70	60	15	18	2	1	2.8946	0.89

From the φ_{in} aspect, on one hand, φ_{in} must keep above zero for ZVS operation. On the other hand, φ_{in} is supposed to be closed enough to zero so that the turn-off current is limited and the primary-side switches achieve quasi-ZCS turning off.

For M_{gain}, since $M_{\mathrm{gain}}(f_{r1})$ is located at around 0.13, the M_{gain} of the rating point f_{sr} should be equal to or above 0.13 in consideration of the rating voltages. In addition, the varying slope of M_{gain} is expected to be mild to weaken the impacts brought by parasites.

Taking the ac voltage stresses into consideration, both V_{C1} and V_{C2} must be restricted. In addition, from (5), V_{C1} and V_{C2} are derived as:

$$V_{\mathrm{C1}} = \left| \sqrt{2} E_{\mathrm{i}} \cdot \frac{V_{\mathrm{C1\text{-}Re1}} + j \cdot V_{\mathrm{C1\text{-}Im1}}}{V_{\mathrm{C1\text{-}Re2}} + j \cdot V_{\mathrm{C1\text{-}Im2}}} \right| \tag{18}$$

$$V_{\mathrm{C2}} = \left| \sqrt{2} E_{\mathrm{i}} \cdot \frac{V_{\mathrm{C2\text{-}Re1}} + j \cdot V_{\mathrm{C2\text{-}Im1}}}{V_{\mathrm{C2\text{-}Re2}} + j \cdot V_{\mathrm{C2\text{-}Im2}}} \right| \tag{19}$$

$$\begin{cases} V_{\mathrm{C1\text{-}Re1}} = 1 \\ V_{\mathrm{C1\text{-}Im1}} = -R_{\mathrm{eq}} B_{\omega} \\ V_{\mathrm{C1\text{-}Re2}} = -\omega_s C_1 A_{\omega} \\ V_{\mathrm{C1\text{-}Im2}} = \omega_s R_{\mathrm{eq}} C_1 (A_{\omega} B_{\omega} + C_{\omega}^2) \end{cases} \tag{20}$$

$$\begin{cases} V_{\mathrm{C2\text{-}Re1}} = R_{\mathrm{eq}} \left(A_{\omega} B_{\omega} + B_{\omega} \dfrac{1 - \omega_s^2 L_1 C_1}{\omega_s C_1} + C_{\omega}^2 - N_1 C_{\omega} \right) \\ V_{\mathrm{C2\text{-}Im1}} = A_{\omega} + \dfrac{1 - \omega_s^2 L_1 C_1}{\omega_s C_1} \\ V_{\mathrm{C2\text{-}Re2}} = R_{\mathrm{eq}} C_1 (A_{\omega} B_{\omega} + C_{\omega}^2) \\ V_{\mathrm{C2\text{-}Im2}} = A_{\omega} \end{cases} \tag{21}$$

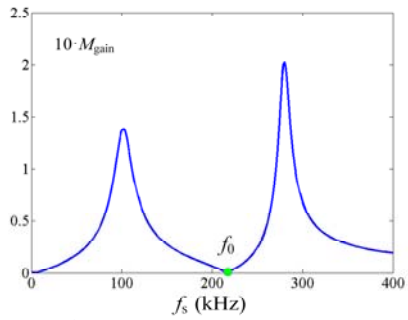

(a)

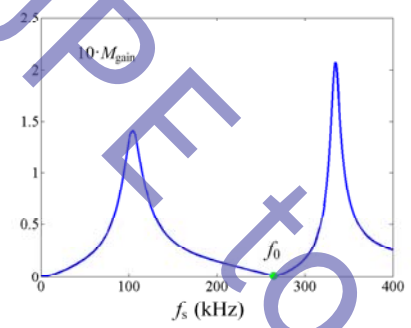

(b)

Fig. 8. RZP positions for different values of C_2: (a) C_2 = 4.5nF; (b) C_2 = 3nF).

Before drawing the 3D figures, the evaluation of C_2 is implemented. From equation (10) it can be known that the RZP f_0 is mainly decided by C_2 and L_2. f_0 is of great significance for a RZP-MERC, since it directly influences the voltage gain range and the operating frequency scope. Thus, f_0 should be in accordance with inequation (3) as analyzed above. However, concerning a small value of C_2, a slight variation of C_2 leads to a large deviation of f_0. When C_2 varies by 1nF, a 11% deviation of f_0 occurs. Meanwhile when L_2 changes by 10μH, only a 5.6% deviation is generated. This phenomenon is illustrated in Fig. 8, where M_{gain} curves are drawn at C_2 = 4.5nF, 3nF. The corresponding RZPs are located at 217kHz and 265kHz, and they both contradict with inequation (3). Under this condition, the proposed converter loses the attractive over-current protection and widely adjustable voltage gain within a narrow frequency band. As a consequence, to avoid a large deviation of f_0, the value of C_2 is fixed at 6nF, which simplifies the following processes.

The relations between φ_{in} and the resonant parameters L_1, L_2 and C_1 are shown in Fig. 9. In Fig. 9a, five surfaces corresponding to C_1 from 3nF to 9nF are presented. Since φ_{in} needs to be above and closed to zero for ZVS operation and low turn-off losses, the demand is only satisfied when C_1 is 6nF, L_2 is from 145μH to 150μH, and L_2 is from 190μH to 200μH. Meanwhile, Fig. 9b illustrates the relation of φ_{in} versus various values of L_1. φ_{in} is kept lower than zero unless C_1 is higher than 6nF, and no obvious relation between φ_{in} and L_1 is found. Thus, in terms of the above analyses, for φ_{in} alone, C_1 should be set at 6nF, and L_1 and L_2 are expected to be located within (190μH, 200μH) and (145μH, 150μH).

TABLE III
OPTIMIZED PARAMETERS AND PRIORITIES

Objective	Optimized Parameters	Priority
Impedance angle φ_{in}	C_1 sets at 6nF L_1 is from 190μH to 200μH L_2 is from 145μH to 150μH	1
Voltage gain M_{gain}	C_1 is from 5nF to 7nF	2
Voltage Stress V_{C1}	Small L_1 C_1 is not within (5nF, 7nF)	3
Voltage Stress V_{C2}	Small L_2 C_1 is not within (5nF, 7nF)	4

TABLE IV
LIST OF OPTIMIZED PARAMETERS

Parameter	Value
Magnetic inductor L_{m1}	300μH
Turns ratio N_1	1.5:1
Magnetic inductor L_{m2}	300μH
Turns ratio N_2	1.5:1
Inductor L_1	190μH
Inductor L_2	145μH
Capacitor C_1	6nF
Capacitor C_2	6nF
Rated operating frequency f_{sr}	100kHz
Rated load R_o	5.4Ω

Fig. 10 shows M_{gain} curves versus L_1, L_2 and C_1. It is clearly shown that M_{gain} reaches its peak values around 0.13 in the scope from 5nF to 7nF. In addition, there are less clues indicating the correlations between M_{gain} and L_1 & L_2. As a result, the C_1 range of 5nF to 7nF is preferred in consideration of M_{gain}.

From the voltage stress aspect, the V_{C1} and V_{C2} curves versus L_1, L_2 and C_1 are shown in Fig. 11 and Fig. 12, respectively. V_{C1} and V_{C2} both reach their peaks during the C_1 range of 5nF to 7nF. For V_{C1}, it rises along with the augment of L_1, and has weak correlation with variations of L_2. Similarly, V_{C2} shows a positive relation with L_2, and it is barely influenced by L_1.

E. Priorities for RCVs

To conclude the 3D figures, for each RCV, and an optimal parameter range can be found without concerning other RCVs. Unfortunately, it is impossible to meet all of the

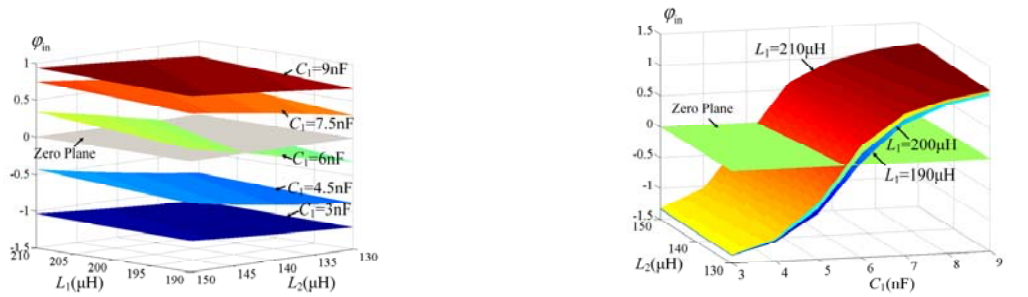

(a) (b)

Fig. 9. Relations of φ_{in} and the resonant parameters. (a) φ_{in} versus L_1 and L_2 at different values of C_1. (b) φ_{in} versus C_1 and L_2 at different values of L_1.

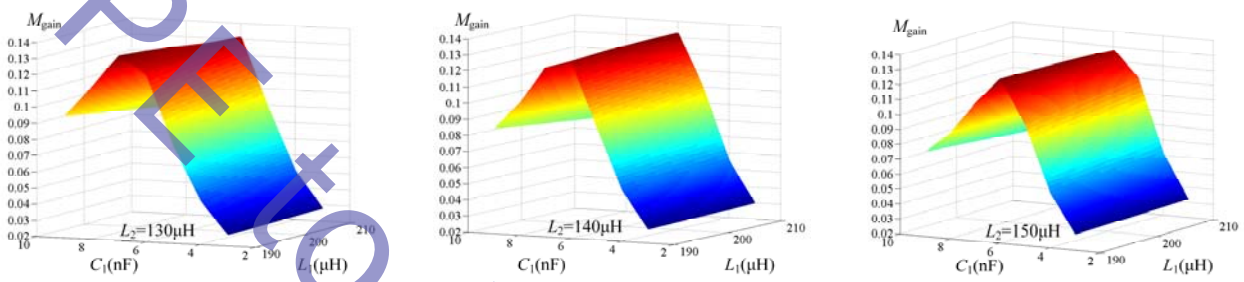

(a) (b) (c)

Fig. 10. Relationships of M_{gain} and the resonant parameters. (a) L_2 = 130μH. (b) L_2 = 140μH. (c) L_2 = 150μH.

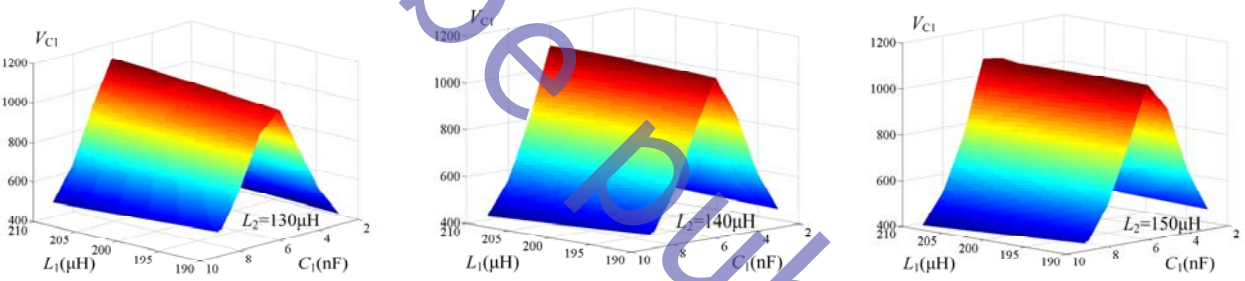

(a) (b) (c)

Fig. 11. Relationships of V_{C1} and the resonant parameters. (a) L_2 = 130μH. (b) L_2 = 140μH. (c) L_2 = 150μH.

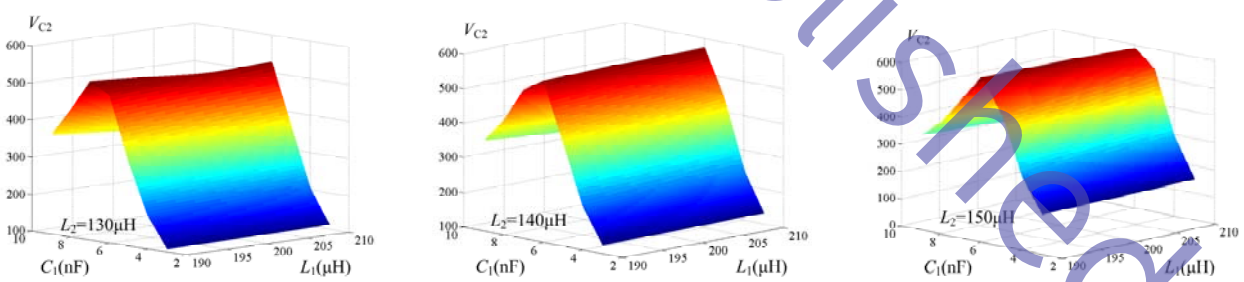

(a) (b) (c)

Fig. 12. Relationships of V_{C2} and the resonant parameters. (a) L_2 = 130μH. (b) L_2 = 140μH. (c) L_2 = 150μH.

demands of the RCVs synchronously, since these optimal ranges may contradict with each other. Accordingly, to deal with this problem, the priority for each of the RCVs is taken into account. The RCV with a higher priority ought to be satisfied at first, since it is more important when compared with the other RCVs. The optimal parameter ranges and priorities for all of the RCVs are listed in Table. III.

φ_{in} has the highest priority since the efficiency issue is of the most importance for dual-CTL converters. Meanwhile, φ_{in} represents the dominant influence on the ZVS turn-on and the quasi-ZCS turn-off losses for the primary-side switches. M_{gain} has the second highest priority, since the rating input and output voltages must be set appropriately. The priorities of the voltage stresses are lower since by applying advanced

switching devices with higher withstand voltages, high voltage stresses can be tolerated despite the rising costs. V_{C1} is much higher than V_{C2}. Therefore, the former ranks higher. At last, concerning Table III, the final resonant parameters are selected and listed in Table. IV.

V. EXPERIMENTS

To verify the practicability of the proposed design method, a 500W dual-CTL prototype was fabricated in the laboratory. Key waveforms and efficiency conditions are tested experimentally.

Fig. 13 presents waveforms under the rating situation, where the voltage v_{S1} and current i_{S1} of the switch S_1, and the voltage v_{SR1} and current i_{SR1} of the SR switch SR_1 are given. Fig. 13(a) indicates that with the chosen parameters, the input impedance angle φ_{in} is confined to a small value above zero. i_{S1} lags almost half a switching cycle behind v_{S1}, which infers the i_{S1} is nearly in phase with the drive signal of S_1. In addition, S_1 fulfills the ZVS turning on and the quasi-ZCS turn-off, since i_{S1} resonates to almost zero when S_1 is turned off. At the same time, SR_1 maintains its inherent ZCS turn-off, and achieves quasi-ZCS turning on due to the small turn-on current. Accordingly, the switching losses is minimized, which contributes to highly efficient conversions.

The voltages across C_1 and C_2 are shown in Fig. 13(b) as v_{C1} and v_{C2}. v_{C1} is made up of two parts. The two parts are a dc component, which is equal to half of the input voltage V_{in}, and an ac component, whose amplitude is V_{C1}. V_{C1} is measured as 1106V and calculated as 1080.9V from (19). The amplitude V_{C2} of v_{C2} is measured as 522V and calculated as 558V. The deviation of V_{C2} is caused by the distortion of v_{C2}.

Waveforms at different operating frequencies are given in Fig. 14, where the input voltage V_{in} is rated at 400V. In Fig. 14(a) and 14(b), f_s is set at 110kHz and 140kHz, respectively. In addition, the corresponding output voltages are 37.2V and 18.3V. φ_{in} increases because f_s is away from the rating point f_{sr}. S_1 loses the quasi-ZCS but still possesses the ZVS turning on. SR_1 maintains the quasi-ZCS turn-on and ZCS turn-off soft-switching.

In Fig. 14(c), with the rating input voltage, the output voltage is only 4.1V at f_s = 183kHz. The voltage gain M_{gain} is around 0.01. Therefore, this frequency is regarded as the RZP f_0. It ensures that the dual-CTL converter possesses the inherent over-current protection and the widely adjustable voltage gain.

The calculations, simulations and experiment results of the dc voltage gain curves are compared in Fig. 15. It can be clearly seen that the threes curves basically match each other from f_{r1} to f_0. When f_s approaches f_{sr}, these curves almost converge to a single point. Meanwhile, when f_s is near f_0, small deviation occurs. This deviation is caused by the intrinsic error of the FHA analysis and parasitic parameters. Fig. 15 shows that the proposed parameter design method has excellent accuracy.

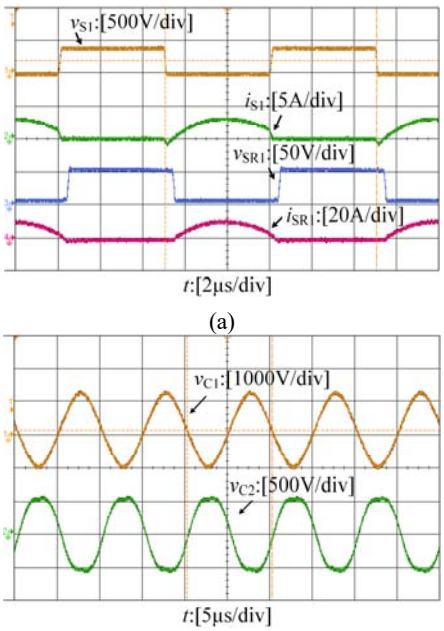

Fig. 13. Waveforms at the rating condition: (a) voltages and currents of S_1 and SR_1; (b) voltages of C_1 and C_2.

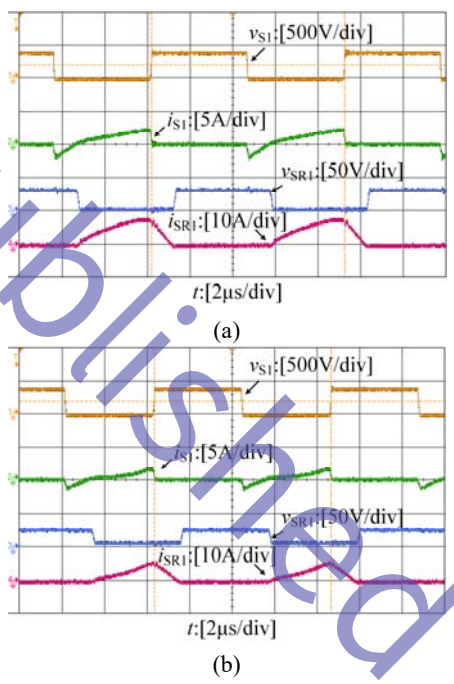

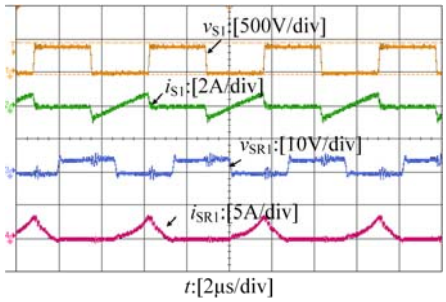

(c)

Fig. 14. Waveforms at different operating frequencies: (a) f_s = 110kHz; (b) f_s = 140kHz; (c) $f_s \approx f_0$ = 183kHz.

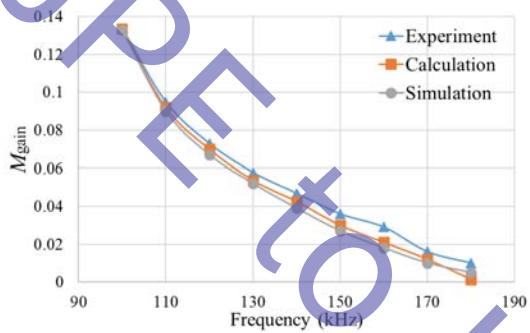

Fig. 15. Comparison of M_{gain} curves.

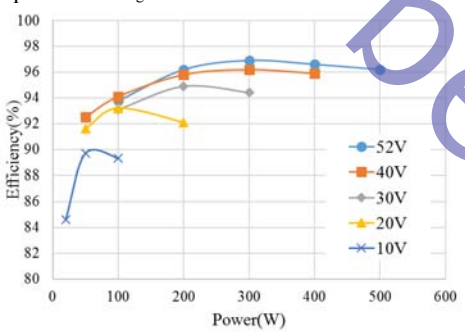

Fig. 16. Efficiency curves with different output voltages.

Efficiency curves with the rating input voltage and different output voltages are given in Fig. 16. Under the rated condition where V_{out} = 52V, the efficiency is at its highest, and the peak value is 96.9% at 300W. This higher efficiency, when compared with similar high step-down RPCs [16], [18], [20], verifies the effectiveness of the designed dual-CTL converter. For other operating states, the efficiency curves inevitably drop due to deviations from the rating point. Despite of this, the converter still maintains a relatively high efficiencies for a wide voltage gain range.

VI. Conclusions

A parameter selection method is proposed for RZP-MERCs in this paper. The main objective of this method is to narrow the acceptable range for all of the variables. Through MATLAB, loss comparisons and 3D figures, the first three steps seek out reasonable parameters within very limited scopes. Then, the last step determines the final resonant parameters by a priority compromise. For different topologies, by altering the selection constraints in the program, it is easy to implant this method on most of the current RZP-MERCs. In addition, a novel dual-CTL MERC is taken as an example to explain the design process. A 500W prototype is established to test the performance. Experiments verify that the proposed converter harvests a wide voltage gain range, limited switching loss, over-current protection and a relatively high efficiency along the entire load range.

References

[1] C. S. Wang, W. Li, Y. F. Wang, F. Q. Han, Z. Meng, and G. D. Li, "An isolated three-port bidirectional DC-DC converter with enlarged ZVS region for HESS applications in DC microgrids," *Energies*, Vol. 10, No. 4, 446, Apr. 2017.

[2] J. H. Han and Y. C. Lim, "Design of an LLC resonant converter for driving multiple LED lights using current balancing of capacitor and transformer," *Energies*, Vol. 8, No. 3, pp. 2125-2144, Mar. 2015.

[3] S. Tian, F. C. Lee, and Q Li, "A simplified equivalent circuit model of series resonant converter," *IEEE Trans. Power Electron.*, Vol. 31, No. 5, pp. 3922-3931, May 2016.

[4] S. Hu, X. Li, M. Lu, and B. Y. Luan, "Operation modes of a secondary-side phase-shifted resonant converter," *Energies*, Vol. 8, No. 11, pp. 12314-12330, Oct. 2015.

[5] R. Beiranvand, B. Rashidian, M. R. Zolghadri, and S. M. H. Alavi, "Optimizing the normalized dead-time and maximum switching frequency of a wide-adjustable-range LLC resonant converter," *IEEE Trans. Power Electron.*, Vol. 26, No. 2, pp. 462-472, Feb. 2011.

[6] R. Beiranvand, B. Rashidian, M. R. Zolghadri, and S. M. H. Alavi, "A Design procedure for optimizing the LLC resonant converter as a wide output range voltage source," *IEEE Trans. Power Electron.*, Vol. 27, No. 8, pp. 3749-3763, Aug. 2012.

[7] R. Yu, G. K. Y. Ho, B. M. H. Pong, B. W. K. Ling, and J. Lam, "Computer-aided design and optimization of high-efficiency LLC series resonant converter. *IEEE Trans. Power Electron.*, Vol. 27, No. 7, pp. 3243-3256, Jul. 2012.

[8] X. Fang, H. Hu, F. Chen, U. Somani, E. Auadisian, J. Shen, and I. Batarseh, "Efficiency-oriented optimal design of the LLC resonant converter based on peak gain placement," *IEEE Trans. Power Electron.*, Vol. 28, No. 5, pp. 2285-2296, May 2013.

[9] J. Tian, J. Gao, and Y. Zhang, "Design of a novel integrated L-C-T for PSFB ZVS converters," *J. Power Electron.*, Vol. 17, No. 4, pp. 905-913, Jul. 2017.

[10] J. W. Kim, J. W. Kim, and G. W. Moon, "A new LLC series resonant converter with a narrow switching frequency variation and reduced conduction losses," *IEEE Trans. Power Electron.*, Vol. 29, No. 8, pp. 4278-4287, Aug. 2014.

[11] Y. Gu, Z. Lu, L. Hang, Z. Qian, and G. Huang, "Three level LLC series resonant DC/DC converter," *IEEE Trans. Power Electron.*, Vol. 20, No. 4, pp. 781-789, Jul. 2005.

[12] H. Wu, T. Xia, X. Zhan, P. Xu, and Y. Xing, "Resonant converter with resonant-voltage- multiplier rectifier and constant-frequency phase-shift control for isolated buck-boost power conversion," *IEEE Trans. Ind. Electron.*, Vol. 62, No. 11, pp. 6974-6985, Nov. 2015.

[13] T. Jiang, J. Zhang, X. Wu, K. Sheng, and Y. Wang, "A bidirectional LLC resonant converter with automatic forward and backward mode transition," *IEEE Trans. Power Electron.*, Vol. 30, No. 2, pp. 757-770, Feb. 2015.
[14] J. Wu, Y. Li, X. Sun, and F. Liu, "A new dual-bridge series resonant DC-DC converter with dual-tank," *IEEE Trans. Power Electron.*, to be published.
[15] Y. Guan, Y. Wang, D. Xu, and W. Wang, "A 1 MHz half-bridge resonant DC/DC converter based on GaN FETs and planar magnetics," *IEEE Trans. Power Electron.*, Vol. 32, No. 4, pp. 2876-2891, Apr. 2017.
[16] M. Mu and F. C. Lee, "Design and optimization of a 380-12V high-frequency, high-current LLC converter with GaN devices and planar matrix transformers," *J. Emerg. Sel. Topics Power Electron.*, Vol. 4, No. 3, pp. 854-862, Sep. 2016.
[17] W. Lee, D. Han, C. T. Morris, and B. Sarlioglu, "High-frequency GaN HEMTs based point-of-load synchronous buck converter with zero-voltage switching," *J. Power Electron.*, Vol. 17, No. 3, pp. 601-609, May 2017.
[18] N. Shafiei, M. Ordonez, M. Craciun, C. Botting, and M. Edington, "Burst mode elimination in high-power LLC resonant battery charger for electric vehicles," *IEEE Trans. Power Electron.*, Vol. 31, No. 2, pp. 1173-1188, Feb. 2016.
[19] J. H. Kim, C. E. Kim, J. K. Kim, J. B. Lee, and G. W. Moon, "Analysis on load-adaptive phase-shift control for high efficiency full-bridge LLC resonant converter under light-load conditions," *IEEE Trans. Power Electron.*, Vol. 31, No. 7, pp. 4942-4955, Jul. 2016.
[20] J. Jang, S. K. Pidaparthy, and B. Choi, "Current mode control for LLC series resonant DC-to-DC converters," *Energies*, Vol. 8, No. 6, pp. 6098-6113, Jun. 2015.
[21] M. T. Outeiro, G. Buja, and D. Czarkowski, "Resonant power converters: an overview with multiple elements in the resonant tank network," *IEEE Ind. Electron. Mag.*, Vol. 10, No. 2, pp. 21-45, Jun. 2016.
[22] H. Hu, X. Fang, F. Chen, Z. J. Shen, and I. Batarseh, "A modified high-efficiency LLC converter with two transformers for wide input-voltage range applications," *IEEE Trans. Power Electron.*, Vol. 28, No. 4, pp. 1946-1960, Jul. 2013.
[23] Z. Liang, R. Guo, J. Li, and A. Q. Huang, "A high-efficiency PV module-integrated DC/DC converter for PV energy harvest in FREEDM systems," *IEEE Trans. on Power Electron.*, Vol. 26, No. 3, pp. 897-909, Mar. 2011.
[24] C. C. Hua, Y. H. Fang, and C. W. Lin, "LLC resonant converter for electric vehicle battery chargers," *IET Power Electron.*, Vol. 9, No. 12, pp. 2369-2376, Jul. 2016.
[25] Y. Du and A. K. S. Bhat, "Analysis and design of a high-frequency isolated dual-tank LCL resonant AC-DC converter," *IEEE Trans. Ind. Appl.*, Vol. 52, No. 2, pp. 1566-1576, Mar./Apr. 2016.
[26] C. Wang, L. Yang, Y. Wang, and B. Chen, "A 1kW CLTCL resonant DC-DC converter with restricted switching loss and broadened voltage range," *IEEE Trans. Power Electron.*, to be published.
[27] H Wu, X. Zhan, and Y. Xin, "Interleaved LLC resonant converter with hybrid rectifier and variable-frequency plus phase-shift control for wide output voltage range applications," *IEEE Trans. Power Electron.*, Vol. 32, No. 6, pp. 4246-4257, Jun. 2017.
[28] J. H. Jung, H. S. Kim, M. H. Ryu, and J. W. Baek, "Design methodology of bidirectional CLLC resonant converter for high-frequency isolation of DC distribution systems," *IEEE Trans. Power Electron.*, Vol. 28, No. 4, pp. 1741-1755, Apr. 2013.
[29] Y. Wang, Y. Guan, D. Xu, and W. Wang, "A CLCL resonant DC/DC converter for two-stage LED driver system," *IEEE Trans. Ind. Electron.*, Vol. 63, No. 5, pp. 2883-2891, May 2016.
[30] X. Qu, S. C. Wong, and C. K. Tse, "An improved LCLC current-source-output multistring LED driver with capacitive current balancing," *IEEE Trans. Power Electron.*, Vol. 30, No. 10, pp. 5783-5791, Oct. 2015.
[31] J. H. Cheng and A. F. Witulski, "Analytic solutions for LLCC parallel resonant converter simplify use of two- and three-element converters," *IEEE Trans. Power Electron.*, Vol. 13, No. 2, pp. 235-243, Mar. 1998.
[32] D. Fu, F. C. Lee, Y. Liu, and M. Xu, "Novel multi-element resonant converters for front-end dc/dc converters," in *Proceedings of the IEEE Power Electronics Specialists Conference*, pp. 250-256, 2008.
[33] J. Koscelnik, M. Prazenica, M. Frivaldsky, and S. Ondirko, "Design and simulation of multi-element resonant LCTLC converter with HF transformer," in *Proceedings of the ELEKTRO*, pp. 307-311, 2014.
[34] T. Mishima, H. Mizutani, and M. Nakaoka, "Experimental evaluations of a five-element multi-resonant dc-dc converter with an improved PFM control range," in *Proceedings of the IEEE International Conference Power Electronics and Drive Systems*, pp. 147-152, 2013.
[35] H. Wu, X. Jin, H. Hu, and Y. Xing, "Multielement resonant converters with a notch filter on secondary side," *IEEE Trans. Power Electron.*, Vol. 31, No. 6, pp. 3999-4004, Jun. 2016.
[36] D. Huang, F. C. Lee, and D. Fu, "Classification and selection methodology for multi-element resonant converters," in *Proceedings of the 26th Annual IEEE Applied Power Electronics Conference and Exposition*, pp. 558~565, 2011.

Yifeng Wang was born in Hubei, China, in 1981. He received his B.S., M.S. and Ph.D. degrees in Electrical Engineering from the Harbin Institute of Technology, Harbin, China, in 2005, 2007 and 2011, respectively. Since 2011, he has been an Associate Professor in the Department of Electrical and Electronics Engineering, Tianjin University, Tianjin, China. His current research interests include the high frequency and soft-switching power converters used for special power supplies, EV chargers, residential photovoltaic grid-connected generation systems, distributed smart wind power generation systems, and the application of power conversion technology to hybrid AC/DC microgrids.

Liang Yang was born in Henan, China, in 1989. He received his B.S. degree in Electrical Engineering from Tianjin University, Tianjin, China, in 2013, where he is presently working towards his Ph.D. degree in Electrical Engineering. His current research interests include small-scale wind generation and high frequency planar magnetic based DC-DC converters.

Guodong Li was born in 1978. He received his B.S. degree in Electrical Engineering from the Northeast Electric Power University, Jilin City, China; and his M.S. degrees in Electrical Engineering from Tianjin University, Tianjin, China. His current research interests include new energy grid-connected detection technologies.

Shijie Tu was born in Jiangxi, China, in 1991. He received his B.S. degree in Electrical Engineering from Tianjin University, Tianjin, China, in 2013. His current research interests include DC-DC converters.